Correspondence to:

V. M. Yarushina,
viktoriya.yarushina@ife.no

Viscous Behavior of Clay-Rich Rocks and Its Role in Focused Fluid Flow

Viktoriya M. Yarushina[1,2] , Roman Y. Makhnenko[3] , Yuri Y. Podladchikov[2,4] , L. Hongliang Wang[1] , and Ludovic Räss[5,6]

[1]Department of Reservoir Technology, Institute for Energy Technology, Kjeller, Norway, [2]Faculty of Mechanics and Mathematics, Moscow State University, Moscow, Russia, [3]Department of Civil & Environmental Engineering, University of Illinois at Urbana-Champaign, Urbana, IL, USA, [4]Institute of Earth Sciences, University of Lausanne, Lausanne, Switzerland, [5]Laboratory of Hydraulics, Hydrology and Glaciology (VAW), ETH Zurich, Zurich, Switzerland, [6]Swiss Federal Institute for Forest, Snow and Landscape Research (WSL), Birmensdorf, Switzerland

Abstract Focused fluid flow is common in sedimentary basins worldwide, where flow structures often penetrate through sandy reservoir rocks, and clay-rich caprocks. To better understand the mechanisms forming such structures, the impacts of the viscoelastic deformation and strongly nonlinear porosity-dependent permeability of clay-rich materials are assessed from an experimental and numerical modeling perspective. The experimental methods to measure the poroviscoelastic and transport properties of intact and remolded shale have been developed, and the experimental data is used to constrain the numerical simulations. It is demonstrated that viscoelastic deformation combined with nonlinear porosity-dependent permeability triggers the development of localized flow channels, often imaged as seismic chimneys. The permeability inside a channel increases by several orders of magnitude compared to the background values. In addition, the propagation time scale and the channel size strongly depend on the material properties of the fluid and the rock. The time-dependent behavior of the clay-rich rock may play a key role in the long-term integrity of the subsurface formations.

1. Introduction

Focused fluid flow is a common phenomenon in shallow and deep Earth. The focused flow in the deep Earth is often evidenced as dikes, veins, volcanic diatremes, or gas venting systems (Minakov et al., 2017; Svensen et al., 2009). In the shallow Earth, it is represented in the form of fluid escape pipes and gas conducting chimneys, mud volcanoes, sand injectites, pockmarks, hydrothermal vent complexes, and others (Berndt, 2005; Judd & Hovland, 2007; Mazzini & Etiope, 2017). While some of the chimneys appear as relict structures in seismic data, observations suggest that others could be relatively young features reaching the present-day seafloor and terminating in pockmarks (Andreassen et al., 2017). Chimney formation continues nowadays, resulting in new impressive structures such as widely publicized 'Siberian mystery craters' (Moskvitch, 2014) or "crazy craters" beneath Swiss Lake Neuchâtel (Reusch et al., 2015). Furthermore, the formation of some chimneys can be associated with industrial fluid injection performed at high fluid pressures. Examples here are the Sleipner CO_2 storage site and wastewater injection experiment in the Tordis Field in the Norwegian North Sea (Arts et al., 2004; Løseth et al., 2011).

Seismic chimneys often indicate vertical hydrocarbon migration from a reservoir or a source rock (Connolly, 2015; Løseth et al., 2009). Shales (fissile claystones) are the most common caprock formations for petroleum reservoirs (Orr, 2009), while intrareservoir claystones can form flow barriers within the host formations, increasing the risk of compartmentalization (e.g., Baz et al., 2016; Mbia et al., 2014) or forming baffles to upward pressure and fluid migration (Bauer et al., 2016). Previous experimental work has shown that claystones exhibit time-dependent or viscous behavior (creep) in response to the applied load (e.g., Sone & Zoback, 2014; Yang et al., 2011; Zhang et al., 2007), and this behavior appeared to be enhanced with increase in relative humidity and pore pressure (Armand et al., 2017; Fabre & Pellet, 2006). Laboratory investigations of claystones' hydromechanical properties are complex because of their low permeability, strong stress-dependence, and high sensitivity to thermal gradients, complicating their characterization (Harrington et al., 2009; Josh et al., 2012).
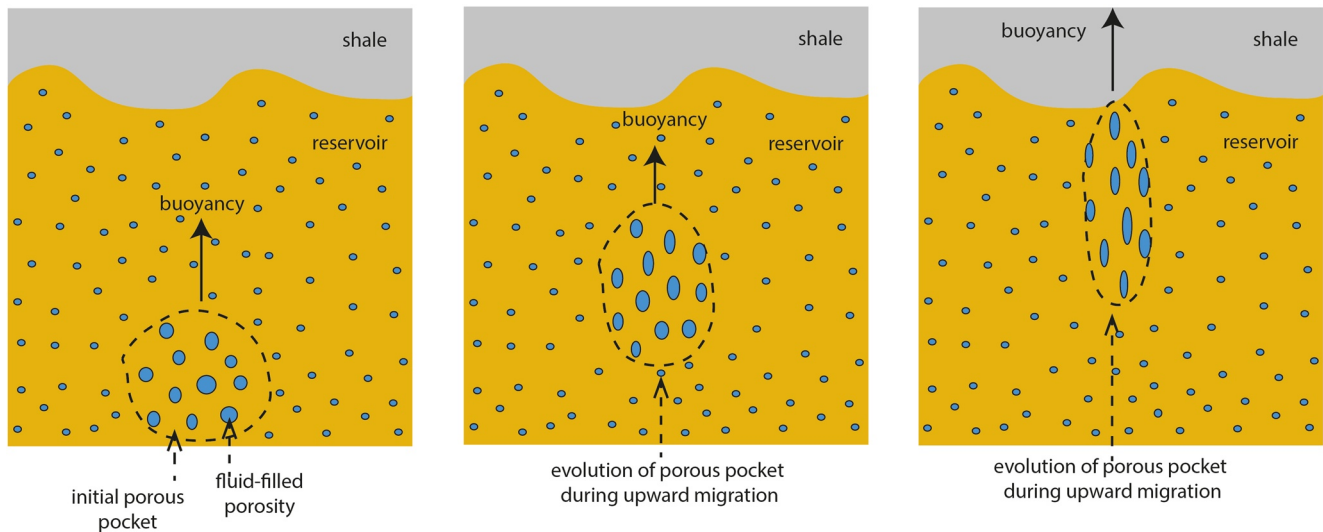
Figure 1. Schematic representation of fluid flow-focusing due to porosity waves mechanism.

Porosity waves were proposed as a potential mechanism of formation of focused fluid flow (Connolly & Podladchikov, 2015; Jordan et al., 2018; Räss et al., 2014, 2018; Richard et al., 2012; Tian & Ague, 2014; Yarushina & Podladchikov, 2015; Yarushina et al., 2015). Previous studies showed that rock viscosity and porosity-dependent permeability are two essential ingredients necessary to generate porosity waves in fluid-saturated rock. Viscoelastic deformation does not require threshold stress and will respond even to a slight increase in fluid pressure. Porosity waves arise as a result of fluid flow instability enhanced by strong interaction between the fluid flow and viscous matrix deformation (Audet & Fowler, 1992; Barcilon & Richter, 1986; Connolly & Podladchikov, 2000; Dohmen et al., 2019; Yarushina et al., 2015). Applied high shear strains (Richardson, 1998; Stevenson, 1989) or ongoing chemical reactions (Omlin et al., 2017) can lead to fluid flow focusing. In the absence of chemical reactions and high shear strains, focusing of the flow occurs due to non-symmetrical dilation and compaction of the pore space, where the latter is delayed compared to its dilation (Connolly & Podladchikov, 2007; Räss et al., 2019; Yarushina et al., 2020). Viscoelastic rocks further sustain the upward propagation of such channels. In general, the direction of the fluid flow is determined by pressure gradient and gravity. The created channels are called "porosity waves" because the solid grains only get displaced locally, allowing fluid transfer through the porous media in a wave-like motion (Figure 1). The size of a single channel formed by the porosity wave depends mainly on the bulk viscosity of the rock, its background permeability, and the shear viscosity of the fluid. In highly permeable rocks featuring large viscosity, one may expect wider channels to form, whereas in tight rocks with low viscosity, channels will be narrow. This dependence is governed by the characteristic compaction length (Mckenzie, 1984). The viscous compaction time scale, which depends on the difference between solid and fluid densities creating buoyancy forces, controls upward channel propagation. Thus, in different geological environments, porosity waves will have different sizes and different propagation times. However, the material parameters critical for accurately assessing porosity waves propagation remain poorly constrained by the available experimental data.

In this study, we perform laboratory experiments on fully saturated intact and remolded Opalinus Clay (Jurassic shale) and measure its poroviscoelastic parameters and permeability at in situ conditions. We use the values obtained in the laboratory experiments as input parameters in the numerical models to predict the time and length scale of possible porosity wave propagation. We present results from more than 600 high-resolution systematic numerical runs to test the influence of physical model parameters and different combinations of porosity within the reservoir and overlying caprock/claystone barrier.

2. Constitutive Model for the Hydromechanical Behavior of Clay-Rich Rock

The hydromechanical behavior of claystones is described in the framework of the poroviscoelastic model of Yarushina and Podladchikov (2015). By extending it to large, irreversible deformations, this model builds on Biot's poroelastic model (Biot, 1941). The governing equations include the standard fluid and solid mass balance, Darcy's law, and momentum conservation. They are complemented with viscoelastic rheological equations in the form:

$$\dot{\varepsilon} = \frac{1}{K_d}\frac{d^s\overline{p}}{dt} - \left(\frac{1}{K_d} - \frac{1}{K_s'}\right)\frac{d^f p_f}{dt} + \frac{\overline{p} - p_f}{(1-\varphi)\eta_\varphi},$$ (1)

$$\frac{d^s\varphi}{dt} = -\left(\frac{1-\varphi}{K_d} - \frac{1}{K_s'}\right)\left(\frac{d^s\overline{p}}{dt} - \frac{d^f p_f}{dt}\right) - \frac{\overline{p} - p_f}{\eta_\varphi},$$ (2)

$$\nabla_k q_k^D = \left(\frac{1}{K_d} - \frac{1}{K_s'}\right)\left(\frac{d^s\overline{p}}{dt} - \frac{1}{B}\frac{d^f p_f}{dt}\right) + \frac{\overline{p} - p_f}{(1-\varphi)\eta_\varphi}.$$ (3)

Here q_i^D are the components of Darcy's flux, which is an incremental analog to Biot's increment of fluid content, φ is the porosity, $\dot{\varepsilon}$ is the volume strain rate, $\overline{p}$, p_f are the total and pore fluid pressures, K_d is the drained bulk modulus, K_s' is the unjacketed bulk modulus, B is Skempton's coefficient, η_φ is the effective bulk viscosity, and d^s/dt and d^f/dt are the Lagrangian derivatives with respect to the solid and the fluid, respectively. Equations 1–3 indicate that the total volume deformation, porosity, and flow are affected by elastic and viscous changes in the total and fluid pressures. The viscous part (the last term) is written in a standard Maxwell viscoelastic manner and governed by Terzaghi's effective mean stress, $p_e = \overline{p} - p_f$. In the purely elastic domain, Equations 1–3 reduce to classical Biot (1941) poroelasticity. Material parameters used by the model can depend on both porosity and pressure, reflecting the nonlinear behavior of clay-rich materials (David et al., 1994; van Noort & Yarushina, 2016, 2019). Here, we adopt the power-law relationship between permeability and the porosity (e.g., Bourbié, 1987):

$$k = k_o\left(\varphi/\varphi_0\right)^n,$$ (4)

where k_0 is a reference permeability at reference porosity φ_0. We solve this mathematical model using a numerical code that ensures accurate coupling between the fluid flow and the geomechanical deformation utilizing a high-resolution grid (Räss et al., 2016, 2018, 2019), which we further use for analysis of the hydromechanical behavior of the clay-rich rocks.

3. Experimental Methods

Poroelastic, poroviscous, and flow parameters are evaluated experimentally using drained, undrained, and unjacketed triaxial compression experiments and steady-state flow tests on intact and remolded shale. Tested Opalinus Clay (shaly facies of Jurassic shale) is a ductile clay-rich material (∼50% clay minerals, 25% calcite, 20% quartz, 5% biodetrius) with a porosity of 0.125, a dominant pore-throat diameter of ∼20 nm (Figure 2a), a permeability of ∼10^{-21} m^2 (Vilarrasa & Makhnenko, 2017).

In the scope of the current study, two types of specimens prepared from shaly facies of Opalinus Clay are investigated: intact (referred to here as shale) and remolded (i.e., reconstituted) rock. The latter may represent the near-surface claystones or material in the proximity of faults and fractures within a shale layer (referred to here as clay) (Egholm et al., 2008). Remolded shale is prepared from crushed intact material, so it is isotropic and has the same mineralogy as Opalinus Clay. The initial porosity of remolded specimens is 0.33, and permeability is ∼10^{-17} m^2, but they decrease to 0.15 and ∼10^{-21} m^2, respectively, at effective mean stresses above 10 MPa (Makhnenko, Vilarrasa, et al., 2017).

Shales, by definition, are fissile rock formations composed of inert mineral inclusions embedded in a clay matrix. The amount of clay is high (>50%), and this determines the very low permeability and sensitivity to water saturation of shales and their chemical composition (Weaver, 1989). Careful specimen preservation after coring (immediate vacuum sealing in thick plastic wraps) allows Opalinus Clay samples to have 0.85 to 0.90 brine saturation, so the natural brine that contains 6.13 g/L of sodium chlorite (NaCl), 1.63 g/L sodium
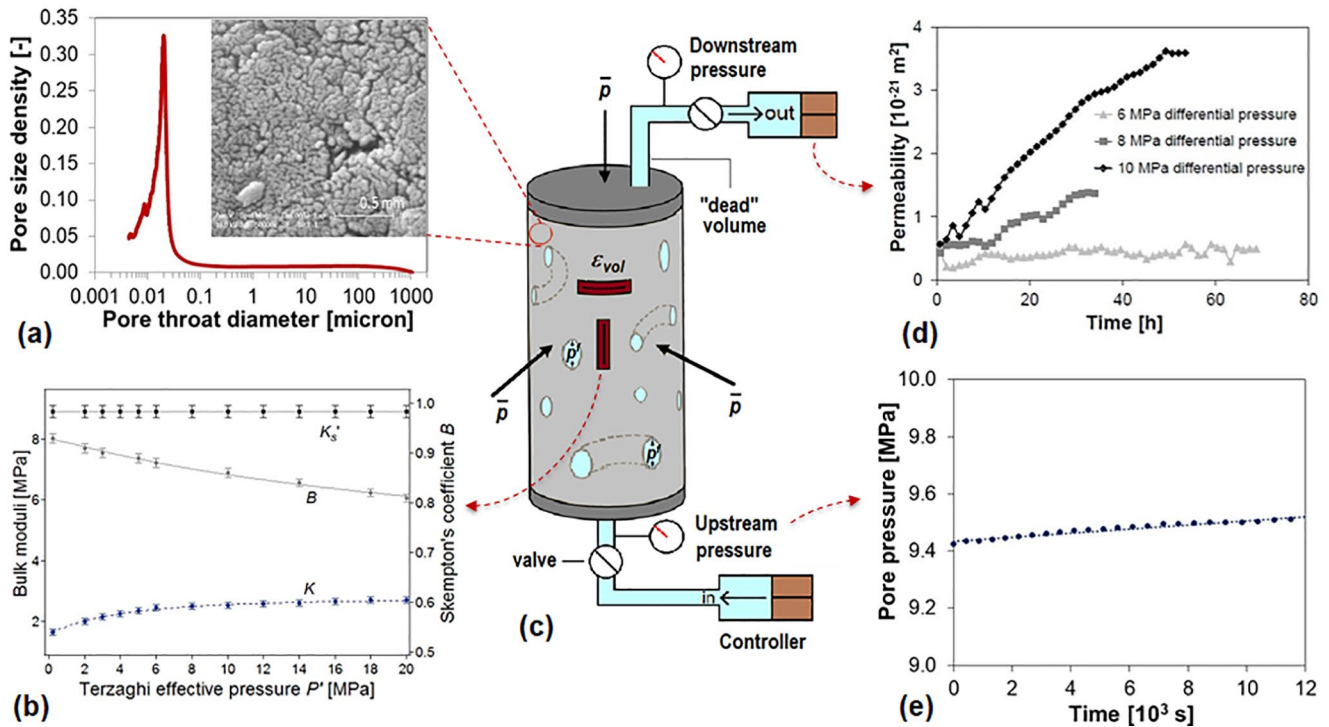
Figure 2. Measurements of shale properties: (a) Pore size distribution (retrieved from mercury intrusion porosimetry) and surface electron microscopy image; (b) Change in volume in the hydrostatic drained compression test (from displacement measurements); (c) Cylindrical specimen with displacement and pore pressure measuring devices; (d) changes of inflow and outflow volumes in steady-state flow permeability test; (e) Pore pressure build-up as a function of time in the undrained test.

sulfate (Na_2SO_4), and traces of other chemicals (Pearson, 2002) with a fluid bulk modulus of $K_f = 2.0$ GPa was used as the pore fluid to minimize the chemical effect. Small dominant pore size determines the low permeability of shale and clay and makes their saturation difficult and experimental times significantly long. All the tested specimens are cored perpendicular to apparent bedding planes–in the direction of the lowest permeability. Only parts of the cores from more than 1 m depth in the gallery are used, with no visible surface cracks. The characteristic time for dissipation of the induced pore pressure in a specimen of length l drained at the two ends is on the order of $l^2/4c$, where c is the diffusion coefficient (Detournay & Cheng, 1993) equal to $10^{-8}\text{m}^2/s$ for the brine-saturated shale (Makhnenko & Podladchikov, 2018). This means that pore pressure diffusion takes tens of hours to be completed in 100 mm long specimens.

The experimental work aims to measure the poroelastic, poroviscous, and flow parameters entering model Equations 1–4. The initial porosity of the materials is accurately determined from mercury intrusion porosimetry tests (Kim & Makhnenko, 2020). Poroelastic parameters, that is, the drained bulk modulus K_d, the unjacketed bulk modulus K'_s, and Skempton's coefficient B, can be measured experimentally under the three limiting conditions: drained, unjacketed, and undrained (Detournay & Cheng, 1993). Another unjacketed parameter, K''_s, is the unjacketed pore modulus. It is excluded from Equation 2 because for Opalinus Clay $K''_s \approx K'_s$ (Makhnenko, Tarokh, & Podladchikov, 2017). The same relationship and value of K'_s are assumed for the remolded shale.

K'_s is measured under the unjacketed boundary conditions, achieved in hydrostatic ($\sigma_1 = \sigma_2 = \sigma_3 = \overline{p}$) compression experiment on prismatic shale specimen ($50 \times 35 \times 35$ mm) instrumented with strain gage rosettes. The experiment is performed in a hydrostatic cell with 10 feedthrough connectors to record the strain gauge readings. Application of 60 MPa fluid pressure for 15 days was required to bring the shale specimen to full saturation. Its unjacketed unloading ($\overline{p} = p_f$ and $d\overline{p} = dp_f$) took 30 days to guarantee pore pressure equilibration inside the rock and proper measurements of K'_s (Makhnenko, Vilarrasa, et al., 2017).
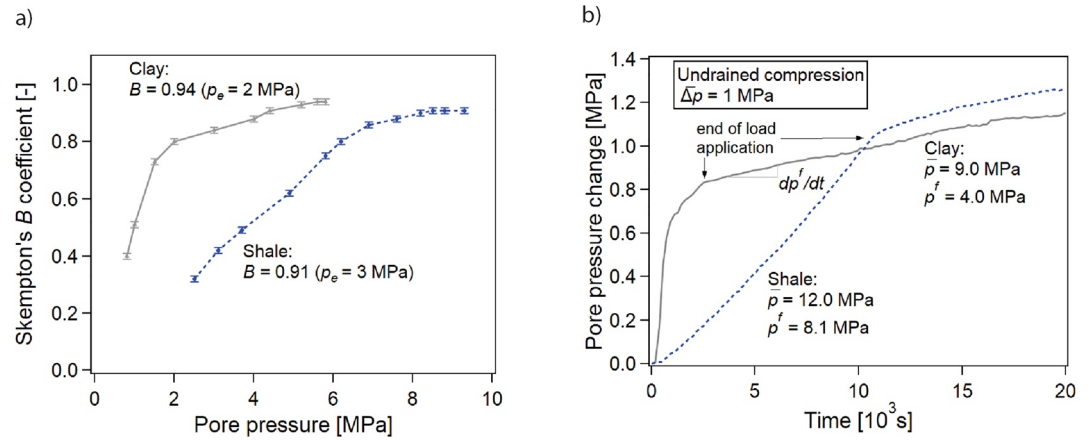
Figure 3. Undrained response of shale and clay: (a) Skempton's B coefficient measurements during the backpressure saturation process, and (b) elastic and viscous pore pressure build-up after achieving full saturation.

Drained (constant pore pressure) and undrained (constant fluid content) compression experiments are conducted on cylindrical specimens (height = 105 mm, diameter = 50 mm, volume = V) in 70 MPa advanced triaxial cell. This cell allows accurate measurements of fluid-saturated rock deformation under different boundary conditions (Makhnenko & Podladchikov, 2018). Backpressure saturation technique is implemented: Skempton's B coefficient is measured at each step of increasing pore pressure at constant mean stress (Wissa, 1969). Achievement of constant value of B corrected for the contribution (about 3%–5%) of the "dead" volume V_L (Figure 2) and the compressibility of the pore pressure measuring system C_{LM}, and independent of the magnitude of the pore pressure indicates full saturation (Bishop, 1976; Ghabezloo & Sulem, 2010):

$$B = \frac{1}{\left(\dfrac{\Delta \bar{p}}{\Delta p_f}\right)^{\text{measured}} - \dfrac{1}{\left(\dfrac{1}{K_d} - \dfrac{1}{K_s'}\right)}\left(\dfrac{V_L}{VK_f} + \dfrac{C_{LM}}{V}\right)} \tag{5}$$

Opalinus Clay, intact and remolded, reaches full saturation with brine (in terms of high and constant measured B values) after a 2-week-long gradual increase of the pore pressure above 8 MPa (Figure 2a). During the application of undrained loading $\nabla q_i^D = 0$, Skempton's B coefficient is affected by the viscous deformation of rock (Equation 3, Figure 3a), so both the pore pressure build-up and the "dead" volume correction have to be taken into account to report "true" B values (Makhnenko & Podladchikov, 2018).

Drained bulk modulus K_d is calculated directly from the measured axial and radial displacements during hydrostatic compression test under constant pore pressure. Pore pressure equilibration in shale after each loading step requires tens of hours. Hence the recorded volume strains are decomposed into elastic and viscous components, Equation 1 with $d^f p_f/dt = 0$. Values of the bulk viscosity η_φ measured in at least three daylong drained tests (where all pore fluid equilibration was over, see below) at the same effective stress are used to calculate K_d from Equation 1 (Makhnenko & Podladchikov, 2018).

The characteristic time scale for equilibration of the pore pressure inside the rock at the range of stresses applied is on the order of 10^5 s for 100 mm long specimens (used in drained tests) and on the order of 10^4 s for the 35 mm long specimen (used in the unjacketed test). In the latter case, though, oil partially penetrated the unjacketed sample and increased the viscosity of the pore fluid, hence, the characteristic time scale for pressure dissipation. After pressure dissipates, it is assumed to be the same everywhere in the specimen because wetting fluid (brine) occupying 90% of the pore space fills the smaller pores. At the same time, oil saturates larger pores where the surface tension effect is on the accuracy of the reported measurements (Makhnenko & Podladchikov, 2018). Finally, each new step in the unjacketed test requires 24 h waiting period, and the whole experiment took 30 days. At least 72 h were spent between the consecutive steps during the drained loading.
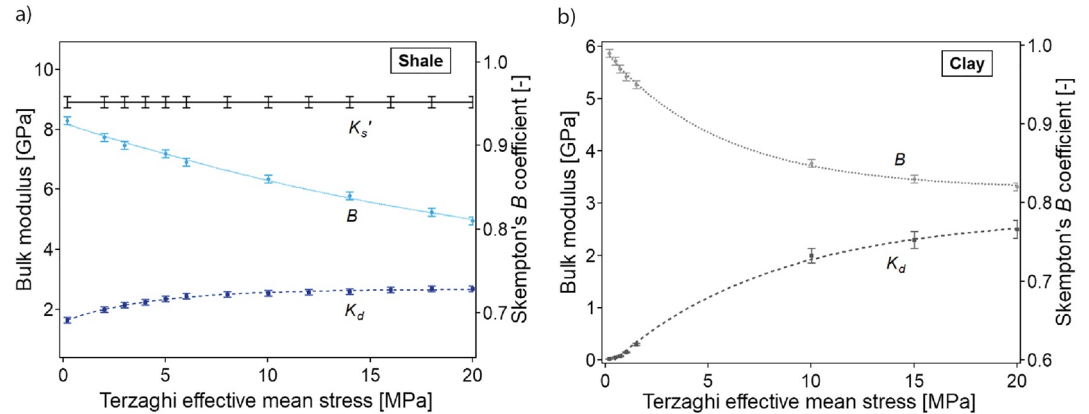
Figure 4. Effective stress-dependent properties of tested rock: (a) unjacketed and drained bulk moduli and Skempton's coefficient for shale; (b) drained bulk modulus and Skempton's coefficient for clay.

When the full saturation is achieved and material deformation is assumed to be poroviscoelastic, no flow ($\nabla_k q_k^D = 0$ or undrained) condition can be considered in Equation 3. In this case, pore fluid pressure build-up with time is predicted at constant total stress conditions (Figure 3b), and it allows for the calculation of the bulk viscosity by the "indirect" method (Makhnenko & Podladchikov, 2018):

$$\eta_\varphi = \frac{B\left(\overline{p} - p_f\right)}{\left(1 - \varphi\right)\dfrac{d^f p_f}{dt}\left(\dfrac{1}{K_d} - \dfrac{1}{K'_s}\right)} \tag{6}$$

Furthermore, the porosity-permeability relationship (Equation 4) is obtained from the measurements of the variation of permeability k with the effective stress p_e. Calculation of porosity assumes the elastic response of rock and the knowledge of the variation of poroelastic properties of shale and clay with the effective stress p_e. The change in porosity $\Delta\varphi$ can be calculated from Equation 2 if the viscous term on the right-hand side is not considered for the short time scales. Plotting k versus φ at different effective stress levels and fitting the data with the power-law function allows calculating the power-law exponent n (Equation 4).

4. Experimental Results

The unjacketed compression test provides constant (stress-independent) values of $K'_s = 8.9$ GPa for intact Opalinus Clay after 30 days of gradual unloading from 60 MPa (Makhnenko, Vilarrasa, et al., 2017). Another specimen is saturated at a pore fluid pressure of 8 MPa in 15 days. It then is gradually loaded in the triaxial cell to total isotropic stress of 10–30 MPa, while its poroviscoelastic parameters are measured (Figure 2). The drained bulk modulus K_d and Skempton's coefficient B show relatively weak stress dependence: $K_d = 1.7 - 2.7$ GPa and $B = 0.81$–0.93 for $p_e = 2 - 20$ MPa (Figure 4a). Remolded shale (clay) appeared to be highly compressible at mean effective stresses <1 MPa ($K_d \approx 10 - 100$ MPa, $B = 0.97$–0.99). However, its bulk modulus became comparable to that of the intact shale at mean effective stresses >10 MPa (Figure 4b).

The brine permeability of shale and clay is measured on fully saturated specimens by the steady-state flow method (Figure 2d). It requires tens of hours for the establishment of the stable flow through a low-permeable clay-rich rock. The injected (inflow) and collected (outflow) volume rates equilibrate after one day of the experiment (both are ≈0.01 ml/day), and longer observation times allow for more accurate permeability measurements. The permeability of shale is found to be strongly stress-dependent, changing from $\sim10^{-20}$ m² to $\sim10^{-21}$ m² for $p_e = 0.2$–20 MPa. Stress dependency is even stronger for clay, where permeability decreases from $\sim10^{-17}$ m² to $3 \cdot 10^{-21}$ m² as the mean stress increases from 0.2 to 20 MPa (Figure 5a). In the presented range of pressures, the permeability dependence on porosity fits well with a power-law relationship, as given by Equation 4, with $k_0 = 8.5 \cdot 10^{-21}$ m², $\varphi_0 = 0.12$, $n = 20$ for shale, and with $k_0 = 5 \cdot 10^{-18}$ m², $\varphi_0 = 0.33$, $n = 8.5$ for clay. The stress- and porosity-dependence of permeability is mainly pronounced at low effective mean stresses.
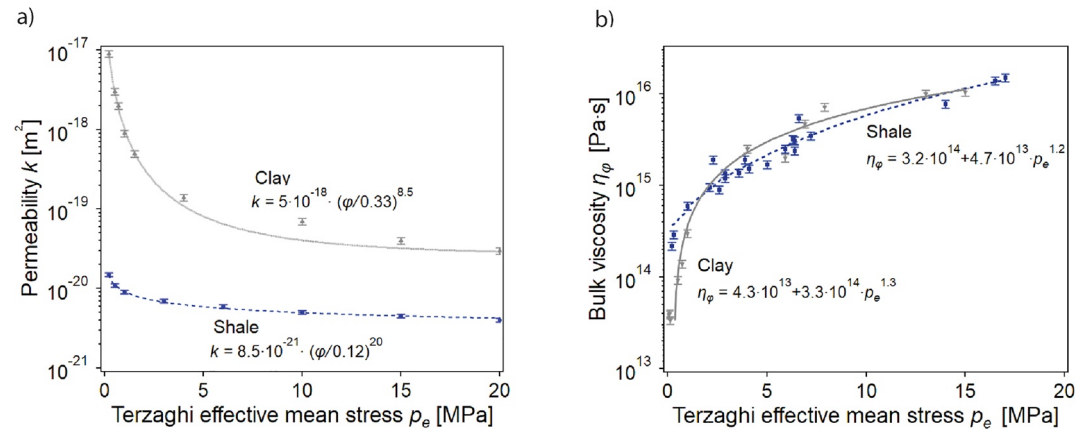
Figure 5. Stress-dependent properties of shale (shaly facies of Opalinus Clay) and clay (remolded Opalinus Clay): (a) permeability and (b) bulk viscosity.

The bulk viscosity values of fully saturated shale and clay are obtained from the undrained data following Equation 6 and are shown in Figure 5b. Considering the temperature dependence of certain shale properties (Räss et al., 2017), all the tests were conducted at 24 ± 0.5°C. The bulk viscosity η_φ for both shale and clay is calculated to be on the order of $10^{15} - 10^{16}\,Pa \cdot s$ at $p_e > 2$ MPa. At lower effective pressures, the value of bulk viscosity drops significantly and appears to be $4 \cdot 10^{13}\,Pa \cdot s$ for clay at $p_e < 0.1$ MPa and $2 \cdot 10^{14}\,Pa \cdot s$ for shale at $p_e < 0.3$ MPa. For both materials, the empirical bulk viscosities can be fitted with a power-law relationship, as shown in Figure 5b. The bulk viscosity values for shale and clay, along with the poroelastic parameters used for calculation, are summarized in Table 1.

It has to be noted that reported bulk viscosities are measured in a somewhat "quazi-static" manner after applying undrained loading. This method showed a very good correlation with the direct measurements of time-dependent volume deformation of fluid-saturated rock on short time scales (hours to days). Still, it may not be very accurate for more extended observations (weeks to months). Additionally, measurements on a few sedimentary rocks showed that η_ϕ was monotonically decreasing with the pore pressure to total mean stress ratio, rather than being a function of effective mean stress (Makhnenko & Podladchikov, 2018).

Table 1
Material Properties for the Tested Shale (Opalinus Clay) and Clay (Remolded Opalinus Clay) at Various Reference States and Associated Length and Time Scales Used in the Model

Material	Test conditions (MPa)	Measured					Calculated			
		$\Phi\,(-)$	$k\,(m^2)$	$K_d\,(GPa)$	$K'_s\,(GPa)$	$B\,(-)$	$c\,(m^2/s)$	$\eta_\varphi\,(Pa{\cdot}s)$	$L\,(m)$	$T\,(year)$
Clay (remolded Opalinus Clay)	$\bar{p} = 1.7$ $p_f = 1.6$	0.30	9×10^{-18}	0.01	8.9	0.99	1.0×10^{-7}	3.4×10^{13}	5.1	9.7
Clay (remolded Opalinus Clay)	$\bar{p} = 2.8$ $p_f = 2.3$	0.28	3×10^{-18}	0.05	8.9	0.98	1.7×10^{-7}	6.4×10^{13}	4.0	23.6
Clay (remolded Opalinus Clay)	$\bar{p} = 19.5$ $p_f = 9.6$	0.15	7×10^{-20}	2.0	8.9	0.86	1.6×10^{-7}	6.0×10^{14}	1.7	497
Shale (Opalinus Clay)	$\bar{p} = 15.0$ $p_f = 14.0$	0.12	9×10^{-21}	1.7	8.9	0.92	1.9×10^{-8}	6.0×10^{14}	0.6	1,680
Shale (Opalinus Clay)	$\bar{p} = 14.0$ $p_f = 7.6$	0.12	6×10^{-21}	2.3	8.9	0.90	1.8×10^{-8}	2.4×10^{15}	1.0	3,390
Shale (Opalinus Clay)	$\bar{p} = 27.0$ $p_f = 10.5$	0.12	4×10^{-21}	2.7	8.9	0.82	1.3×10^{-8}	1.4×10^{16}	1.8	12,100

5. Porosity Waves in Claystones

Previous research has shown that a combination of viscous rock deformation and porosity-dependent permeability may lead to the formation of solitary porosity waves (Barcilon & Richter, 1986; Connolly & Podladchikov, 1998; Richard et al., 2012). Porosity waves in the context of sedimentary basins and focused fluid flow systems were studied by Appold and Nunn (2002), Audet and Fowler (1992), Connolly and Podladchikov (2000), Joshi et al. (2012), Revil (2002), and Yarushina et al. (2020). In this section, the numerical approach to modeling the focused fluid flow is described and demonstrated with applications to the tested claystones.

It is customary in numerical modeling to introduce non-dimensional parameters. In viscous porous models, a natural depth scale to choose is that over which porosity changes significantly. It is given by the compaction length, L, defined as (Mckenzie, 1984)

$$L = \sqrt{\frac{\eta_0 k_0}{\mu_f}}. \tag{7}$$

The time scale is given by the viscous compaction time,

$$T = \frac{\eta_0}{L\Delta\rho g}, \tag{8}$$

The characteristic pressure scale is

$$P = \Delta\rho g L \tag{9}$$

where $\Delta\rho$ is the difference in solid and fluid densities creating buoyancy forces, η_0 is the reference solid shear viscosity, and g is the gravitational acceleration. The viscosity and density of pore fluid might vary significantly depending on the type and composition of the fluid, pressure, and temperature. For natural gas, the viscosity is on the order of $10^{-5} \mathrm{Pa} \cdot \mathrm{s}$, and density ranges between $7 - 300 \mathrm{kg/m^3}$ for temperatures between $37°$ and $170°C$ and pressures between 6.8 and 550 MPa (Lee et al., 1966). For brine, the viscosity varies between $1.5 \cdot 10^{-3} - 30 \cdot 10^{-3}$ Pa · s, and density is about $900 - 1,100 \mathrm{kg/m^3}$ (Francke & Thorade, 2010). Liquid CO_2-in-water emulsions have viscosity on the order $10^{-3} \mathrm{Pa} \cdot \mathrm{s}$ and density of $900 - 1,000 \mathrm{kg/m^3}$ (Wu et al., 2021). The characteristic scales L and T in this work are calculated for illustration purposes assuming viscosity and density of natural gas from Lee et al. (1966). The obtained values are summarized in Table 1. Since the viscosity and density of most of the fluids depend both on temperature and pressure, the characteristic scales might vary upon the depth and local conditions.

To demonstrate the influence of the experimentally derived material parameters on porosity waves, we consider a domain featuring a boundary between the reservoir and a caprock representative of shale or clay-rich barrier. The size of the domain is $20L \times 60L$ (Figure 6), where L depends on the properties of the rock and ranges between 0.6 and 5.1 m for the natural gas (see Table 1). We impose free-slip boundary conditions for the solid velocities (no shear stress and zero normal velocity). For the fluid flow problem, we assign no flux conditions on the lateral boundaries. Vertical inflow (bottom) and outflow (top) values are chosen to satisfy zero effective pressure at the bottom and top boundaries to prevent the occurrence of compaction or decompaction (see Section 3 in Räss et al. [2019] for further details). The only external force acting on the domain is the downward pointing gravity.

We base our simulations on the model of porous fluid flow in deformable viscoelastoplastic rocks by Yarushina and Podladchikov (2015), briefly summarized in Section 2. The effective bulk viscosity η_φ accounts for the nonlinear dependence on the shear stresses and decompaction weakening, here parametrized by a hyperbolic tangent function (Räss et al., 2019):

$$\eta_\varphi = \frac{\eta_0}{\varphi} \frac{1}{1 + (\tau_{II}/\tau_0)^{m-1}} \left[1 + \frac{1}{2}\left(\frac{1}{R} - 1\right)\left(1 - \tanh\frac{p_e}{\lambda}\right) \right] \tag{10}$$

where τ_{II} is the square root of the second invariant of the deviatoric stress tensor, τ_0 is the characteristic stress, m is the viscous power-law exponent, λ is the transition zone sharpness between the compacting and decompacting regime, and $R = \eta_c/\eta_d$ is a rheological constant quantifying the ratio of compaction bulk viscosity (at $p_e \gg \lambda$) over decompaction (at $p_e \ll -\lambda$). For symmetric viscosity producing blob-like porosity waves, $R = 1$. In our simulations, we use $R = 10^5$, resulting in decompaction weakening (see Table 2 for
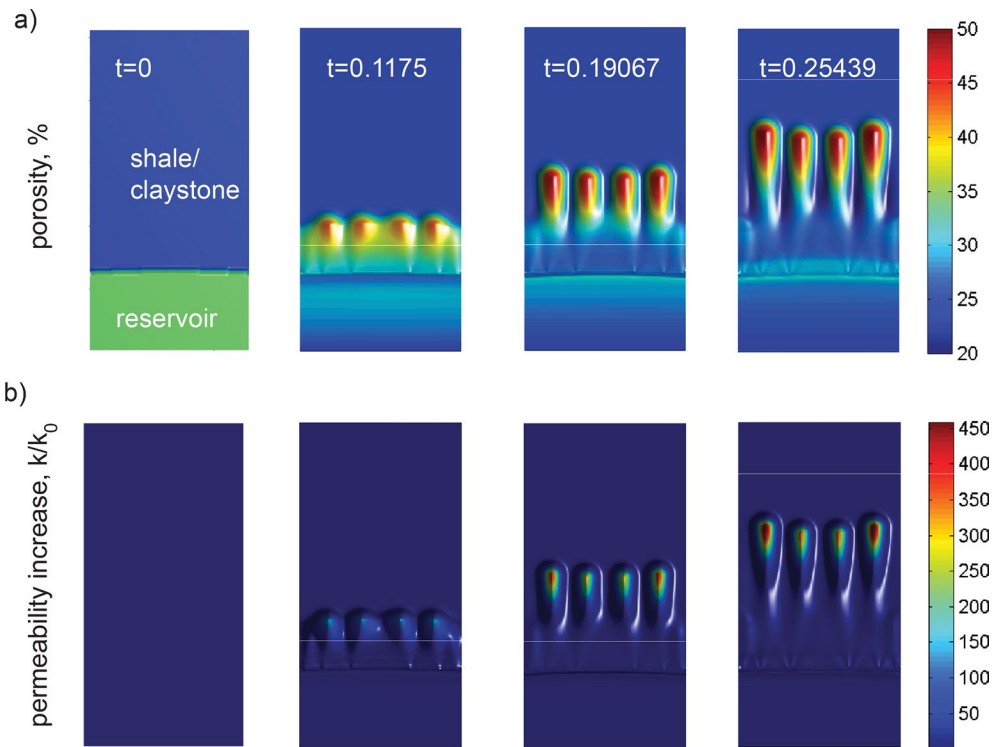
Figure 6. Formation of enhanced flow channels caused by porosity waves propagation in clay with initial porosity of $\varphi_0 = 0.25$, reservoir porosity $\varphi_r = 0.35$, $m = 3$, and $n = 8.5$ shown in snapshots of porosity at different time steps: (a) porosity and (b) permeability increase (k/k_0) within the channel with respect to the background value for the same run; time is scaled with the characteristic time T described in the text. The domain extent is $20L \times 60L$.

other parameters). The complete set of equations implemented in the numerical code is described in detail in Räss et al. (2019). We rely on a finite-difference discretization and employ a second-order pseudo-transient relaxation approach to achieve an implicit solution of the nonlinear coupled system of equations (Omlin et al., 2018; Räss et al., 2016, 2019). Extremely high values of permeability exponent n, observed in our laboratory experiments and supported by some previous works (e.g., Dong et al. [2010]) indicate very strong coupling between deformation and fluid flow that require careful numerical treatment justifying a two-way (or full) coupling strategy.

Significant non-linearity of porosity-permeability relationship associated with large values of n is challenging for numerical simulations. We ensure the convergence of the global residual for the full nonlinear and coupled system at each time step to guarantee the accuracy of the results. The simulation results are independent of space and time scale, as shown in Räss et al. (2019, 2016). We systematically vary reservoir porosity and values of permeability exponent n between 2.5 and 40. We motivate this choice by the observations from the flow and mechanical tests on shale-like materials that report n to vary between 7 and 50 (Dong et al., 2010; Kim & Makhnenko, 2020; Revil & Cathles, 1999). Huge porosity variations and almost nine orders of magnitude increase in permeability (Figure 9b) associated with channel formation create additional numerical challenges. They require very high spatial resolution to capture the channel dynamics. The numerical algorithm is written in C-CUDA and runs on Nvidia GPUs to efficiently process in parallel 0.25 billion grid points. More than 600 nonlinear high-resolution runs ($1,023 \times 3,071$ cells) are performed on 128 GPUs (Nvidia GTX Titan X Maxwell) in parallel on the octopus supercomputer. This machine, hosted by the Swiss Geocomputing Center, Institute of Earth Sciences, University of Lausanne, Switzerland, was in-house designed for

Table 2
Non-Dimensional Simulation Parameters

Description	Symbol	Value
Characteristic stress	τ_0	10^8
Viscous power-law exponent	m	3 or 8
Transition zone sharpness compaction/decompaction	λ	0.01
Decompaction weakening factor	R	10^5
Density ratio	ρ_s/ρ_f	2
Bulk to shear solid viscosity ratio	η_0/μ_s	10
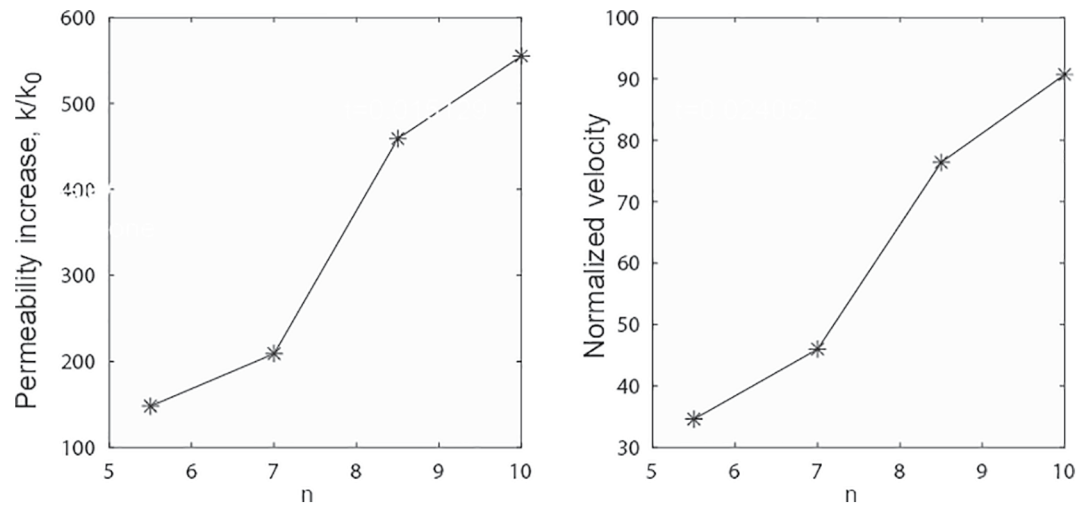
Figure 7. Results from a parametric study showing the dependence of permeability increase inside a channel and the velocity of its upward propagation on permeability exponent, n, for clay with initial porosity of $\varphi_0 = 0.25$ and reservoir porosity $\varphi_r = 0.35$ at $m = 3$. Velocity is normalized by the background Darcy velocity $V_{Darcy} = k_0(\rho_s - \rho_f)g/\mu_f$.

such high-performance computations. We test the influence of physical model parameters and different combinations of porosity within the reservoir and overlying caprock/claystone barrier.

5.1. Clay

For the caprock consistent of the clay, we assumed homogeneous porosity $\varphi_0 = 0.25$, which lies within the range reported in Table 1. We consider the underlying sandy reservoir with a typical porosity of $\varphi_r = 0.35$ as reported, for instance, for Utsira or Skade sand formations in the North Sea (Elenius et al., 2018). We made systematic variations of n between 3 and 10. Other fixed parameters used in simulations are summarized in Table 2. Numerical simulations show that flow instability first leads to initial disaggregation of the fluid flow front (Figure 6a). With time, several distinct fluid channels are formed, with characteristic size and spacing. Such instability is driven by buoyancy forces only and thus does not require elevated fluid pressures in the reservoir. Pressure grows locally at the top of the channel so that the initial reservoir pressure generally remains low. The size of a single channel formed by the porosity wave depends mainly on the bulk viscosity of the rock, η_φ, its background permeability, k_0, and the fluid shear viscosity, μ_f, that is, on the compaction length, L. In highly permeable and viscous rock, one might expect wider channels to form, whereas channels will be narrow in tight rock with low viscosity.

The propagation of porosity waves is characterized by a localized significant increase of porosity and permeability. For the example shown in Figure 6, porosity within the channel reaches 0.51, which is much higher than the initial porosity of the reservoir or clay barrier above the reservoir. Permeability within the channel is calculated to be up to 458 times higher than the initial background value. The permeability increase within the channel follows the evolution of porosity (Figure 6b). It is controlled by the degree of coupling between the fluid flow and deformation, as described by the permeability exponent n. Higher non-linearity leads to a more pronounced increase in permeability, which reaches values in the range of $k/k_0 = 147 - 555$ for $n = 5.5 - 10$ (Figure 7). It is interesting to note that permeability increase inside a channel non-linearly depends on the permeability exponent, that is, its growth slows down with higher n.

In 3-D, the created channels appear as circular cylindrical bodies (Räss et al., 2014, 2018). Their diameters vary between 2 and 3.8 times the compaction length L. Depending on the depth and pressure in the reservoir, the expected diameter of a channel is ∼2.4–19.4 m in clay. By converting non-dimensional values of the velocity of upward channel growth shown in Figure 7 into dimensional values using the characteristic time and length scales T and L from Table 1, we obtain that channels grow at a velocity of ∼0.1–47 m/year in clay. The lower estimate corresponds to values obtained for $p_e = 9.9$ MPa and $n = 5.5$, that is, for a relatively deep case. The upper estimate corresponds to the $p_e = 0.1$ MPa and $n = 10$, that is, shallower or overpressured
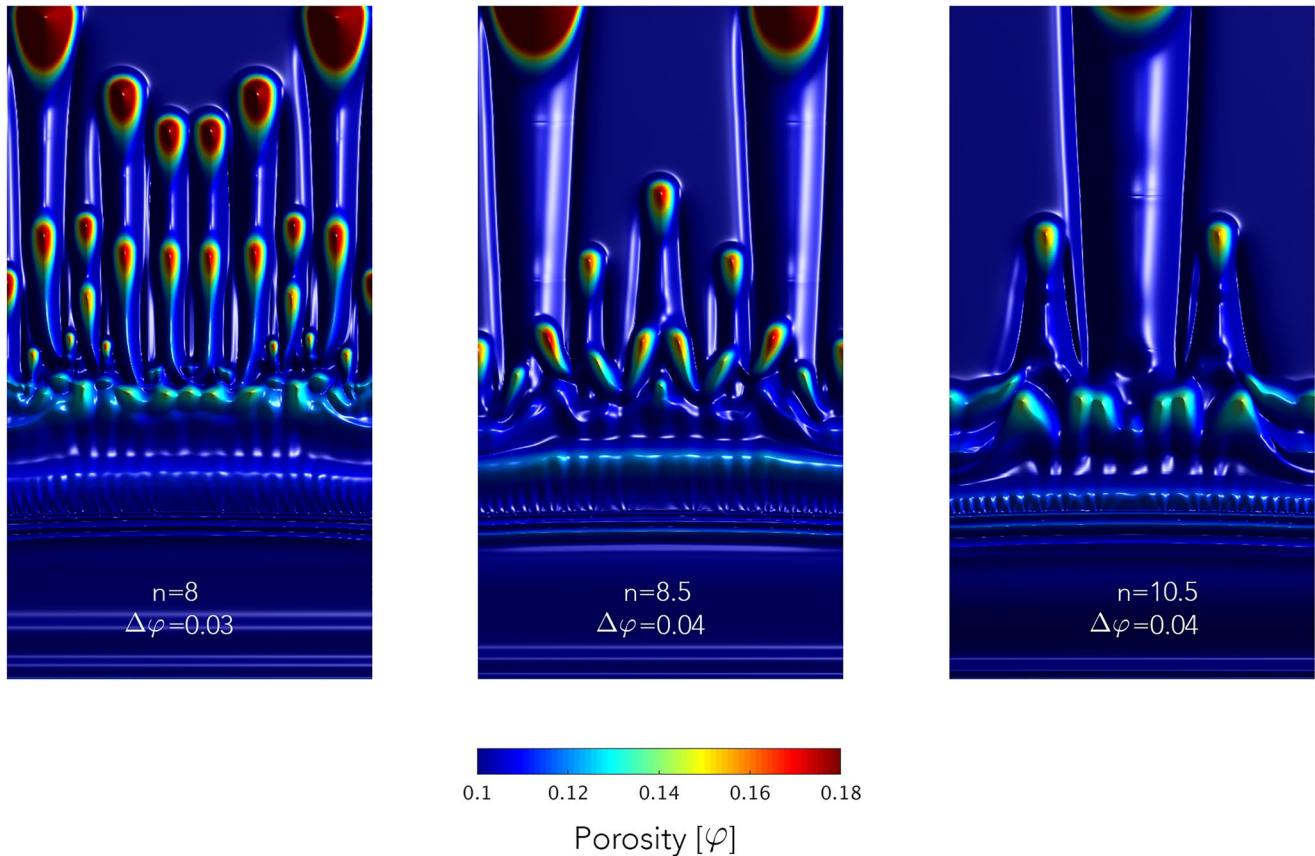
Figure 8. Different patterns of channel formation in the shaly caprock. The colors represent the porosity values obtained for different n and $\Delta\varphi$ as indicated in each plot for $m = 8$.

conditions. It will only take several months to penetrate through 1 m of clay barriers in the latter case. At the same time, for clay with higher permeability and bulk viscosity than those considered here, the formation of channels of a larger size might be expected. In this case, individual channels might become visible on seismic images as narrow zones of deteriorated quality in the form of gas chimneys or fluid-escape pipes.

5.2. Shale

Shales have, in general, lower porosity than clays. Thus, for the simulations of the fluid flow through the shale caprock, a homogeneous initial porosity of shale $\varphi_0 = 0.1$ is assumed. In shales, the degree of coupling between the flow and deformation is even higher than in clay reflecting in much higher values of $n = 2.5 - 40$. We also want to test the effect of the porosity difference between the reservoir and a caprock, $\Delta\varphi = \varphi_r - \varphi_0$, on the flow. For this reason, the reservoir porosity is systematically varied in the range $\varphi_r = 0.11 - 0.15$. Given that higher non-linearity leads to a more pronounced increase in porosity, we limit ourselves to this relatively small range of reservoir porosities to avoid numerical problems related to the extremely high non-linearity of the flow.

The channels formed in shale follow various patterns that have one or a few larger channels accompanied by several smaller channels (Figure 8). The number of channels depends on the permeability exponent and the difference between reservoir and caprock porosity, $\Delta\varphi$ (Figure 9a). Shales with higher non-linearity of permeability, i.e., larger values of n, tend to form few but larger channels. The same effect has a difference between reservoir and caprock porosity. Reservoirs with higher $\Delta\varphi$ tend to produce a few large channels, while reservoirs with smaller $\Delta\varphi$ produce a large number of smaller channels. Assuming compaction length L ranging between 0.6 and 1.8 m, the width of the channel in the shale might vary between 1.2 and 6.84 m. The velocity of its upward migration would be on the order of 0.03–1.3 m/yr based on the values of L and
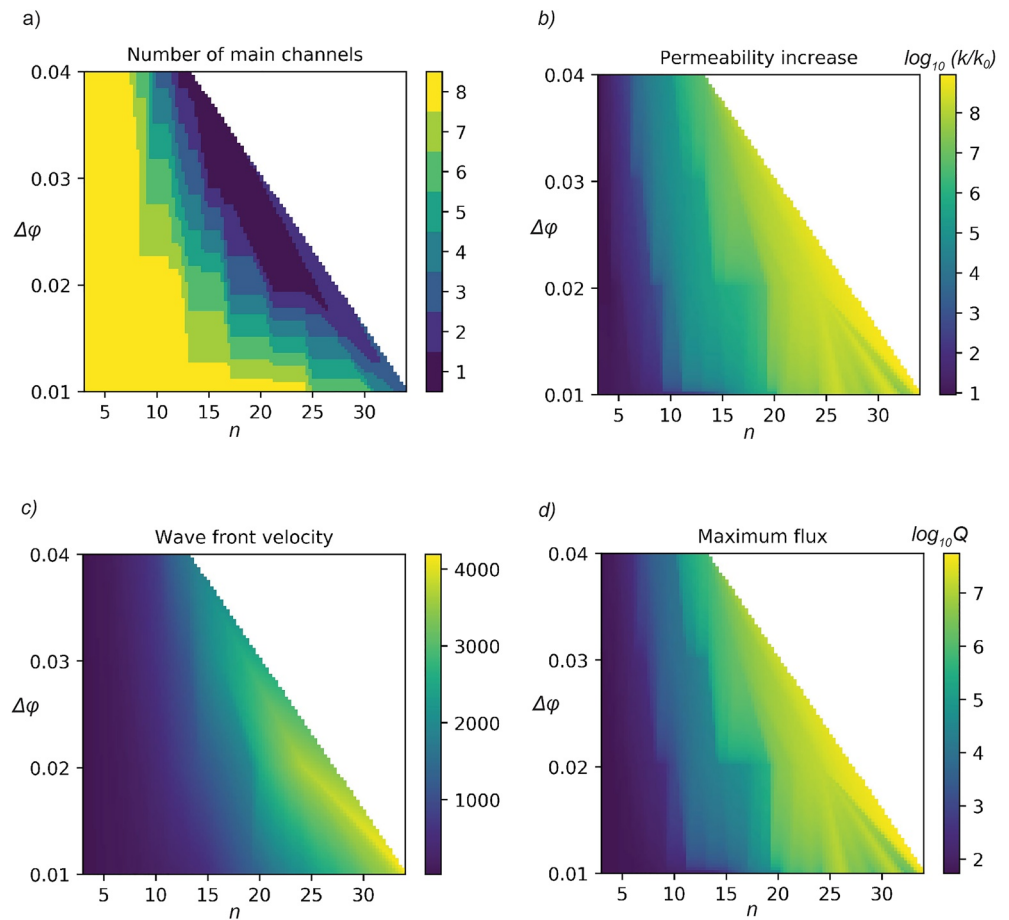
Figure 9. Results from a systematic investigation that shows the dependence of channel formation and their hydraulic properties on the difference between reservoir and shale porosities $\Delta\varphi$ and permeability exponent n. Demonstrated values represent (a) number of produced large channels, (b) maximum permeability increase within one channel on a logarithmic scale in comparison with the initial background values, $\log_{10}k/k_0$, (c) non-dimensional maximum velocity of upward channel growth, VT/L, and (d) the maximum vertical fluid-percolation flux through the entire horizontal cross-section Q normalized by the background Darcy velocity V_{Darcy} and compaction length L.

T given in Table 1 and Figure 8c. The lower value corresponds to the case of $p_e = 16.5$MPa, $\Delta\varphi = 0.01$, and $n = 4$. The higher value corresponds to parameter values measured for $p_e = 1$MPa and simulations performed at $\Delta\varphi = 0.01$ and $n = 35$. Assuming a moderate speed of 50 mm/year, it will take ~1,300 years to penetrate through 100 m of nearly impermeable shale. Indeed, observations indicate that thick shale sequences are often pierced by seismic chimneys (Aminzadeh et al., 2001; Gay et al., 2007; Heggland, 1998; Løseth et al., 2011; Nourollah et al., 2010; Vadakkepuliyambatta et al., 2013).

The velocity depends on material parameters such as permeability and the initial porosity difference between reservoir and caprock (Figure 9c). Variations in L and T with depth and pressure might lead to channel growth at faster or slower velocities. For gas, the density difference $\Delta\rho$ will be larger, increasing the velocity of wave propagation. The ratio between the compaction and dilation viscosity, R, also affects the rate of channel propagation. At elevated temperatures and pore pressures close to lithostatic, the bulk viscosity of the clay-rich formation reduces significantly, thus promoting faster channel propagation.

The permeability within the channel k depends on the background permeability of the formation k_0, as well as $\Delta\varphi$ and n (Figure 9b). For large values of n, permeability k within the channel might increase by seven orders of magnitude compared to its background value k_0. Thus, nearly impermeable shale with $k_0 \sim 10^{-21}$ m^2 might have channels with the permeability of $k \sim 10^{-14}$ m^2. This extreme permeability increase makes porosity waves the preferential fluid flow pathways.

Our numerical results show that one episode of chimney formation will bring a limited amount of fluid from the reservoir, and then a channel will tend to close. However, porosity in its wake is still slightly higher than the background values. New channels that form later tend to use the channels that were created earlier (Figure 8). This process will make a persisting chimney, where fluid escape might be episodic. In addition, channel behavior strongly depends on the rheology of the surrounding rocks (Connolly & Podladchikov, 1998; Yarushina et al., 2015). Irreversible plastic deformation, which was not considered in our simulations, will work against the channel's closure once the bubble has passed and will help sustain the channel for a prolonged time even if there is no major fluid escape.

Fluid flux through a given horizontal cross-section of the computational domain associated with the channel formation can be estimated as $Q = \int_{\Sigma} q_D^y \, d\Sigma$. Its values normalized by the Darcy velocity of the background fluid flow $V_{Darcy} = k_0(\rho_s - \rho_f)g/\mu$ and compaction length L are provided in Figure 9d. They show similar dependence on $\Delta\varphi$ and n as permeability and wave velocity. When converted to dimensional numbers based on the T and L given in Table 1, they result in $Q = 0.03$ to $8 \cdot 10^{13}$ m^3/yr per 1 m^2.

6. Discussion

6.1. Porosity Waves and Model Assumptions

To better understand the physics behind porosity waves, simplified set of equations for a particular case when shear stresses are ignored and $\overline{p}$ is assumed to be lithostatic can be considered

$$\frac{d\varphi}{dt} = -\frac{\overline{p} - p_f}{\eta_\varphi} + \frac{1}{K_\varphi}\left(\frac{dp_f}{dt} - \frac{d\overline{p}}{dt}\right) \tag{11}$$

$$\frac{1}{K_\varphi}\frac{d\left(p_f - \overline{p}\right)}{dt} = \nabla\left(\frac{k(\varphi)}{\mu_f}\left(\nabla\left(p_f - \overline{p}\right) - \Delta\rho g\right)\right) + \frac{\overline{p} - p_f}{\eta_\varphi} \tag{12}$$

Equation 11 is a modified Equation 2, where $1/K_\varphi = (1 - \varphi)/K_d - 1/K_s'$. Equation 12 is a usual pressure diffusion equation in viscoelastic rocks in the presence of gravity forces (Connolly & Podladchikov, 1998; Detournay & Cheng, 1993). Buoyancy force arising from the second term on the right-hand side of diffusion equation ($\Delta\rho g$) leads to fluid pressure build-up even without additional fluid injection. This, in turn, leads to porosity growth and upward fluid migration. The nonlinear nature of the diffusion equation arising from porosity dependence of permeability gives rise to fluid flow instability leading to the generation of porosity waves (Figure 6).

To understand the relative importance of viscous and elastic terms, it is helpful to rewrite Equation 11 in the non-dimensional form, assuming that K_φ has a weak dependence on porosity and stress

$$\frac{d\varphi}{dt} = -De\frac{d\tilde{p}_e}{dt} - \frac{\tilde{p}_e}{\tilde{\eta}_\varphi} \tag{13}$$

where $\tilde{\eta}_\varphi = \eta_\varphi/\eta_0$ is a non-dimensional viscosity, $\tilde{p}_e$ is the non-dimensional effective pressure, and $De = \eta_0/(TK)$ is the Deborah number (Connolly & Podladchikov, 1998). Equation 13 shows that the Deborah number determines the relative importance of elastic versus viscous compaction. Given elastic and viscous parameters summarized in Table 1, we obtain that Deborah number ranges from $6 \cdot 10^{-6}$ to 10^{-2}. Thus, the viscous term will dominate for clays and shales considered in this study, and elastic deformation can be ignored. Elasticity will dominate for large values of $De \sim 1$.

Porosity increase within the channel is associated with local pressure build-up at the channel's top, leading to decompaction. This local pressure build-up is limited by the effective pressure at which pore space starts to dilate. Equation 11 shows that in purely viscous rocks ($K_\varphi \rightarrow \infty$), dilation will happen at p_f exceeding total lithostatic pressure $\overline{p}$. However, the presence of elastic and plastic deformation will lead to dilation at $p_f < \overline{p}$ (Yarushina et al., 2020).

Our simulations used the effective viscosity with decompaction weakening given by Equation 10, predicting viscosity drop at low effective pressures approaching zero. We do not consider dilating regime in our experiments. Under hydrostatic loading conditions of our experiment, it would require fluid pressures exceeding confining pressure, which is practically not feasible at the current technology level. Yet, our experimental results

show a significant viscosity drop at low effective pressures (Figure 5b). Recent work by Sabitova et al. (2021) addressed both compacting and dilating regimes under triaxial testing conditions. It confirmed that time-dependent deformation rates, and thus viscosities, are different during compaction and decompaction.

6.2. Important Applications

Focused fluid flow in hydrocarbon-bearing sedimentary basins is primarily evidenced using reflection seismic as near-vertical zones of highly attenuated chaotic data, called "gas chimneys" or "fluid-escape pipes." Chimneys and pipes are common features observed at sub-seabed sediments in continental margins. They were found offshore Norway in actively producing hydrocarbon fields (e.g., Albuskjell, Ekofisk, Eldfisk, Hod, Nyegga, Tommeliten, and Vallhall), as well as offshore Africa, Australia, and in the Gulf of Mexico (Arntsen et al., 2007; Bunz et al., 2012; Gay et al., 2007; Moss & Cartwright, 2010; Nourollah et al., 2010; Ostanin et al., 2013). The presence of seismic chimneys has been proposed as an indicator for deeper prospective hydrocarbon reservoirs (Aminzadeh et al., 2001; Heggland, 1998). In many cases, chimney structures can be traced down to gas/oil-rich reservoirs and up to the seafloor or surface, where they form craters or pockmarks. Interestingly, they often penetrate through sandy reservoir rocks as well as through nearly impermeable shaley caprocks. Well data obtained inside and outside a gas chimney reveals that chimneys have an increased fluid pressure compared to the background levels (Løseth et al., 2011). Our results explain these observations and provide the physical mechanism of seismic chimneys penetrating through reservoir seals and shaley caprocks.

The role of carbon capture and storage as an effective climate mitigation technology depends on our ability to store large volumes of carbon dioxide (CO_2) securely in geological formations for tens of thousands of years. Secure storage means no CO_2 leakage to the near-surface and no noticeable effects on the ground infrastructure in the form of induced seismicity. Various trapping mechanisms operating in the subsurface, such as structural and stratigraphic barriers or dissolution and capillary forces, work together to keep CO_2 from escaping back to the atmosphere (Metz et al., 2005). Still, the buoyancy of CO_2, combined with its acidity and potential thermo-hydro-mechanical effects, may lead to CO_2 leakage across the caprock. For example, during the first three years of operation at the Sleipner field storage pilot in the North Sea (Norway), CO_2 propagated upward through several thin mudstone barriers with a total thickness of 17 m (Cavanagh & Haszeldine, 2014), even though the predicted CO_2 entry pressures for the caprock were significantly above the induced overpressure. The repeated seismic surveys identified several seismic chimneys in the Sleipner storage site.

Our results suggest that focused fluid flow structures form very fast on the geological time scales. This is indeed indirectly supported by observations. Among them, reports on the formation of the seafloor crater within few months after the start of wastewater injection (Løseth et al., 2011) and on the formation of seismic chimneys within few days in the controlled CO_2 injection experiments from the QICS project (Cevatoglu et al., 2015).

7. Conclusions

Clay-rich materials are common caprocks and seals that hinder upward fluid migration. Yet, focused fluid flow structures are commonly observed above them. The properties of clay-rich rocks are strongly stress- and time-dependent. Our experiments demonstrate viscous compaction and provide values of bulk viscosity on the order of 10^{13}–10^{16} Pa·s for claystone and remolded shale. Our modeling results show that viscous rock deformation strongly coupled with the fluid flow may lead to the development of vertical channels of focused fluid flow within clay barriers and shaly caprocks. Using values of bulk viscosity and permeability obtained in laboratory experiments for two representative materials, we predict channels formed by natural gas to propagate at a velocity of 0.1–47 m/year in the clay and a rate of 0.03–1.3 m/year in shale. Their diameters would range between 2 and 19 m in clay and between 1 and 7 m in shale. The permeability within the channel may increase up to nine orders of magnitude compared to the intact rock. Estimated fluid flux associated with the formation of a channel based on the material parameters provided by our experimental data is in the order of 0.03 to $8 \cdot 10^{13}$ m³/yr per 1 m². The chimneys' formation is possible over the hydrocar-

bon reservoirs and CO_2 storage sites, so the local conditions and material properties have to be carefully examined to avoid any potential leakages.

Data Availability Statement

The numerical code used in this study is available for download from Bitbucket at https://bitbucket.org/lraess/m2di and the Swiss Geocomputing Centre website https://wp.unil.ch/geocomputing/software/. The experimental data is available from Viscous behavior of clay-rich rocks and its role in focused fluid flow | Zenodo.

References

Aminzadeh, F., de Groot, P., Berge, T., & Valenti, G. (2001). Using gas chimneys as an exploration tool. *World Oil*, *222*(5), 69–72.

Andreassen, K., Hubbard, A., Winsborrow, M., Patton, H., Vadakkepuliyambatta, S., Plaza-Faverola, A., et al. (2017). Massive blow-out craters formed by hydrate-controlled methane expulsion from the Arctic seafloor. *Science*, *356*(6341), 948–953. https://doi.org/10.1126/science.aal4500

Appold, M. S., & Nunn, J. A. (2002). Numerical models of petroleum migration via buoyancy-driven porosity waves in viscously deformable sediments. *Geofluids*, *2*(3), 233–247. https://doi.org/10.1046/j.1468-8123.2002.00040.x

Armand, G., Conil, N., Talandier, J., & Seyedi, D. M. (2017). Fundamental aspects of the hydromechanical behaviour of Callovo-Oxfordian claystone: From experimental studies to model calibration and validation. *Computers and Geotechnics*, *85*, 277–286. https://doi.org/10.1016/j.compgeo.2016.06.003

Arntsen, B., Wensaas, L., Loseth, H., & Hermanrud, C. (2007). Seismic modeling of gas chimneys. *Geophysics*, *72*(5), Sm251–Sm259. https://doi.org/10.1190/1.2749570

Arts, R., Eiken, O., Chadwick, A., Zweigel, P., van der Meer, L., & Zinszner, B. (2004). Monitoring of CO_2 injected at Sleipner using time-lapse seismic data. *Energy*, *29*(9–10), 1383–1392. https://doi.org/10.1016/j.energy.2004.03.072

Audet, D. M., & Fowler, A. C. (1992). A mathematical-model for compaction in sedimentary basins. *Geophysical Journal International*, *110*(3), 577–590. https://doi.org/10.1111/j.1365-246X.1992.tb02093.x

Barcilon, V., & Richter, F. M. (1986). Nonlinear-waves in compacting media, *Journal of Fluid Mechanics*, *164*, 429–448. https://doi.org/10.1017/S0022112086002628

Bauer, R. A., Carney, M., & Finley, R. J. (2016). Overview of microseismic response to CO_2 injection into the Mt. Simon saline reservoir at the Illinois Basin-Decatur Project. *International Journal of Greenhouse Gases Control*, *54*, 378–388. https://doi.org/10.1016/j.ijggc.2015.12.015

Baz, H., Noureldin, M., Allinson, W. G., & Cinar, Y. (2016). A field-scale investigation of residual and dissolution trapping of CO_2 in a saline formation in Western Australia. *International Journal of Greenhouse Gases Control*, *46*, 86–99. https://doi.org/10.1016/j.ijggc.2015.12.032

Berndt, C. (2005). Focused fluid flow in passive continental margins. *Philosophical Transactions of the Royal Society A*, *363*(1837), 2855–2871. https://doi.org/10.1098/rsta.2005.1666

Biot, M. A. (1941). General theory of three-dimensional consolidation. *Journal of Applied Physics*, *12*(2), 155–164. https://doi.org/10.1063/1.1712886

Bishop, A. W. (1976). Influence of system compressibility on observed pore pressure response to an undrained change in stress in saturated rock. *Géotechnique*, *26*(2), 371–375. https://doi.org/10.1680/geot.1976.26.2.371

Bourbié, T. (1987). *Acoustics of porous media* (Vol. 16, p. 334). Editions Technip.

Bunz, S., Polyanov, S., Vadakkepuliyambatta, S., Consolaro, C., & Mienert, J. (2012). Active gas venting through hydrate-bearing sediments on the Vestnesa Ridge. *Marine Geology*, *332*, 189–197. https://doi.org/10.1016/j.margeo.2012.09.012

Cavanagh, A. J., & Haszeldine, R. S. (2014). The Sleipner storage site: Capillary flow modeling of a layered CO_2 plume requires fractured shale barriers within the Utsira Formation. *International Journal of Greenhouse Gases Control*, *21*, 101–112. https://doi.org/10.1016/j.ijggc.2013.11.017

Cevatoglu, M., Bull, J. M., Vardy, M. E., Gernon, T. M., Wright, I. C., & Long, D. (2015). Gas migration pathways, controlling mechanisms and changes in sediment acoustic properties observed in a controlled sub-seabed CO_2 release experiment. *International Journal of Greenhouse Gases Control*, *38*, 26–43. https://doi.org/10.1016/j.ijggc.2015.03.005

Connolly, D. L. (2015). Visualization of vertical hydrocarbon migration in seismic data: Case studies from the Dutch North Sea. *Interpretation-J Sub*, *3*(3), Sx21–Sx27. https://doi.org/10.1190/Int-2015-0007.1

Connolly, J. A. D., & Podladchikov, Y. Y. (1998). Compaction-driven fluid flow in viscoelastic rock. *Geodinamica Acta*, *11*(2–3), 55–84. https://doi.org/10.1016/S0985-3111(98)80006-5

Connolly, J. A. D., & Podladchikov, Y. Y. (2000). Temperature-dependent viscoelastic compaction and compartmentalization in sedimentary basins. *Tectonophysics*, *324*(3), 137–168. https://doi.org/10.1016/s0040-1951(00)00084-6

Connolly, J. A. D., & Podladchikov, Y. Y. (2007). Decompaction weakening and channeling instability in ductile porous media: Implications for asthenospheric melt segregation. *Journal of Geophysical Research: Solid Earth*, *112*(B10), B10205. https://doi.org/10.1029/2005jb004213

Connolly, J. A. D., & Podladchikov, Y. Y. (2015). An analytical solution for solitary porosity waves: Dynamic permeability and fluidization of nonlinear viscous and viscoplastic rock. *Geofluids*, *15*(1–2), 269–292. https://doi.org/10.1111/gfl.12110

David, C., Wong, T. F., Zhu, W. L., & Zhang, J. X. (1994). Laboratory measurement of compaction-induced permeability change in porous rocks - Implications for the generation and maintenance of pore pressure excess in the crust. *Pure and Applied Geophysics*, *143*(1–3), 425–456. https://doi.org/10.1007/Bf00874337

Detournay, E., & Cheng, A. H. D. (1993). Fundamentals of poroelasticity. In J. A. Hudson (Ed.), *Comprehensive rock engineering: Principles, practice and projects* (pp. 113–171). Pergamon Press. https://doi.org/10.1016/b978-0-08-040615-2.50011-3

Dohmen, J., Schmeling, H., & Kruse, J. P. (2019). The effect of effective rock viscosity on 2-D magmatic porosity waves. *Solid Earth*, *10*(6), 2103–2113. https://doi.org/10.5194/se-10-2103-2019

Dong, J. J., Hsu, J. Y., Wu, W. J., Shimamoto, T., Hung, J. H., Yeh, E. C., et al. (2010). Stress-dependence of the permeability and porosity of sandstone and shale from TCDP Hole-A. *Chem Erde-Geochem*, *47*(7), 1141–1157. https://doi.org/10.1016/j.ijrmms.2010.06.019

Egholm, D. L., Clausen, O. R., Sandiford, M., Kristensen, M. B., & Korstgard, J. A. (2008). The mechanics of clay smearing along faults. *Geology*, *36*(10), 787–790. https://doi.org/10.1130/G24975a.1

Elenius, M., Skurtveit, E., Yarushina, V., Baig, I., Sundal, A., Wangen, M., et al. (2018). Assessment of CO_2 storage capacity based on sparse data: Skade Formation. *International Journal of Greenhouse Gases Control*, *79*, 252–271. https://doi.org/10.1016/j.ijggc.2018.09.004

Fabre, G., & Pellet, F. (2006). Creep and time-dependent damage in argillaceous rocks. *Internatonal Journal of Rock Mechanics and Mineral Science*, *43*(6), 950–960. https://doi.org/10.1016/j.ijrmms.2006.02.004

Francke, H., & Thorade, M. (2010). Density and viscosity of brine: An overview from a process engineers perspective. *Chem Erde-Geochem*, *70*, 23–32. https://doi.org/10.1016/j.chemer.2010.05.015

Gay, A., Lopez, M., Berndt, C., & Seranne, M. (2007). Geological controls on focused fluid flow associated with seafloor seeps in the Lower Congo Basin. *Marine Geology*, *244*(1–4), 68–92. https://doi.org/10.1016/j.margeo.2007.06.003

Ghabezloo, S., & Sulem, J. (2010). Effect of the volume of the drainage system on the measurement of undrained thermo-poro-elastic parameters. *Internatonal Journal of Rock Mechanics and Mineral Science*, *47*(1), 60–68. https://doi.org/10.1016/j.ijrmms.2009.03.001

Harrington, J. F., Noy, D. J., Horseman, S. T., Birchall, D. J., & Chadwick, R. A. (2009). Laboratory study of gas and water flow in the Nordland Shale, Sleipner, North Sea. In M. Grobe, J. C. Pashin, & R. J. Dodge (Eds.), *Carbon dioxide sequestration in geological media – State of the Science* (pp. 521–543).

Heggland, R. (1998). Gas seepage as an indicator of deeper prospective reservoirs. A study based on exploration 3D seismic data, *Marine and Petroleum Geology*, *15*(1), 1–9. https://doi.org/10.1016/S0264-8172(97)00060-3

Jordan, J. S., Hesse, M. A., & Rudge, J. F. (2018). On mass transport in porosity waves. *Earth and Planetary Science Letters*, *485*, 65–78. https://doi.org/10.1016/j.epsl.2017.12.024

Josh, M., Esteban, L., Delle Piane, C., Sarout, J., Dewhurst, D. N., & Clennell, M. B. (2012). Laboratory characterisation of shale properties. *Journal of Petroleum Science and Engineering*, *88–89*, 107–124. https://doi.org/10.1016/j.petrol.2012.01.023

Joshi, A., Appold, M. S., & Nunn, J. A. (2012). Evaluation of solitary waves as a mechanism for oil transport in poroelastic media: A case study of the South Eugene Island field, Gulf of Mexico basin. *Marine and Petroleum Geology*, *37*(1), 53–69. https://doi.org/10.1016/j.marpetgeo.2012.06.011

Judd, A. G., & M. Hovland, (2007). *Seabed Fluid Flow : The Impact of Geology, Biology and the Marine Environment* (Vol. 15, p. 475). Cambridge University Press.

Kim, K., & Makhnenko, R. Y. (2020). Coupling between poromechanical behavior and fluid flow in tight rock. *Transport in Porous Media*, *135*(2), 487–512. https://doi.org/10.1007/s11242-020-01484-z

Lee, A. L., Gonzalez, M. H., & Eakin, B. E. (1966). Viscosity of natural gases, *Journal of Petroleum Technology*, *18*(8), 997–1000. https://doi.org/10.2118/1340-Pa

Løseth, H., Gading, M., & Wensaas, L. (2009). Hydrocarbon leakage interpreted on seismic data. *Marine and Petroleum Geology*, *26*(7), 1304–1319. https://doi.org/10.1016/j.marpetgeo.2008.09.008

Løseth, H., Wensaas, L., Arntsen, B., Hanken, N. M., Basire, C., & Graue, K. (2011). 1000 m long gas blow-out pipes. *Marine and Petroleum Geology*, *28*(5), 1047–1060. https://doi.org/10.1016/j.marpetgeo.2010.10.001

Makhnenko, R. Y., & Podladchikov, Y. Y. (2018). Experimental poroviscoelasticity of common sedimentary rocks. *Journal of Geophysical Research: Solid Earth*, *123*(9), 7586–7603. https://doi.org/10.1029/2018jb015685

Makhnenko, R. Y., Tarokh, A., & Podladchikov, Y. Y. (2017). On the unjacketed moduli of sedimentary rock. *Poromechanics VI: Proceedings of the Sixth Biot Conference on Poromechanics* (pp. 897–904).

Makhnenko, R. Y., Vilarrasa, V., Mylnikov, D., & Laloui, L. (2017). Hydromechanical aspects of CO_2 breakthrough into clay-rich caprock. *Energy Procedia*, *114*, 3219–3228. https://doi.org/10.1016/j.egypro.2017.03.1453

Mazzini, A., & Etiope, G. (2017). Mud volcanism: An updated review. *Earth-Science Reviews*, *168*, 81–112. https://doi.org/10.1016/j.earscirev.2017.03.001

Mbia, E. N., Frykman, P., Nielsen, C. M., Fabricius, I. L., Pickup, G. E., & Sorensen, A. T. (2014). Modeling of the pressure propagation due to CO_2 injection and the effect of fault permeability in a case study of the Vedsted structure, Northern Denmark. *International Journal of Greenhouse Gas Control*, *28*, 1–10. https://doi.org/10.1016/j.ijggc.2014.06.006

Mckenzie, D. (1984). The generation and compaction of partially molten rock. *Journal of Petrology*, *25*(3), 713–765. https://doi.org/10.1093/petrology/25.3.713

Metz, B., Davidson, O., & De Coninck, H. (Eds.). (2005). *Carbon dioxide capture and storage: Special report of the intergovernmental panel on climate change*. Cambridge University Press.

Minakov, A. V., Yarushina, V. M., Faleide, J. I., Krupnova, N., Sakoulina, T., Dergunov, N., & Glebovsky, V. (2017). *Dyke emplacement and crustal structure within a continental large igneous province - northern Barents Sea*. Geological SocietySpecial Publications.

Moskvitch, K. (2014). *Mysterious Siberian crater attributed to methane*. Nature News and Comment. https://doi.org/10.1038/nature.2014.15649

Moss, J. L., & Cartwright, J. (2010). The spatial and temporal distribution of pipe formation, offshore Namibia. *Marine and Petroleum Geology*, *27*(6), 1216–1234. https://doi.org/10.1016/j.marpetgeo.2009.12.013

Nourollah, H., Keetley, J., & O'Brien, G. (2010). Gas chimney identification through seismic attribute analysis in the Gippsland Basin, Australia. *The Leading Edge*, *29*, 896–901. https://doi.org/10.1190/1.3479999

Omlin, S., Malvoisin, B., & Podladchikov, Y. Y. (2017). Pore fluid extraction by reactive solitary waves in 3-D. *Geophysical Research Letters*, *44*(18), 9267–9275. https://doi.org/10.1002/2017gl074293

Omlin, S., Räss, L., & Podladchikov, Y. Y. (2018). Simulation of three-dimensional viscoelastic deformation coupled to porous fluid flow. *Tectonophysics*, *746*, 695–701. https://doi.org/10.1016/j.tecto.2017.08.012

Orr, F. M. (2009). Onshore geologic storage of CO_2. *Science*, *325*(5948), 1656–1658. https://doi.org/10.1126/science.1175677

Ostanin, I., Anka, Z., di Primio, R., & Bernal, A. (2013). Hydrocarbon plumbing systems above the Snohvit gas field: Structural control and implications for thermogenic methane leakage in the Hammerfest Basin, SW Barents Sea. *Marine and Petroleum Geology*, *43*, 127–146. https://doi.org/10.1016/j.marpetgeo.2013.02.012

Pearson, F. J. (2002). *PC experiment: Recipe for artificial pore water* (Report). Mont Terri Project. Technical Note 2002–17.

Räss, L., Duretz, T., & Podladchikov, Y. Y. (2019). Resolving hydromechanical coupling in two and three dimensions: Spontaneous channelling of porous fluids owing to decompaction weakening. *Geophysical Journal International*, *218*(3), 1591–1616. https://doi.org/10.1093/gji/ggz239

Räss, L., Makhnenko, R., Podladchikov, Y. Y., & Laloui, L. (2017). Quantification of viscous creep influence on storage capacity of caprock. *Energy Procedia*, *114*, 3237–3246.

Räss, L., Simon, N. S. C., & Podladchikov, Y. Y. (2018). Spontaneous formation of fluid escape pipes from subsurface reservoirs. *Scientific Reports*, *8*. https://doi.org/10.1038/s41598-018-29485-5

Räss, L., Yarushina, V., Duretz, T., & Podladchikov, Y. (2016). High-resolution numerical modelling to resolve the dynamics of pipe structures in porous media. *Paper presented at ECMOR XV - 15th European Conference on the Mathematics of Oil Recovery.*

Räss, L., Yarushina, V. M., Simon, N. S. C., & Podladchikov, Y. Y. (2014). Chimneys, channels, pathway flow or water conducting features - An explanation from numerical modelling and implications for CO_2 storage. *Energy Procedia*, *63*, 3761–3774. https://doi.org/10.1016/j.egypro.2014.11.405

Reusch, A., Loher, M., Bouffard, D., Moernaut, J., Hellmich, F., Anselmetti, F. S., et al. (2015). Giant lacustrine pockmarks with subaqueous groundwater discharge and subsurface sediment mobilization. *Geophysical Research Letters*, *42*, 3465–3473. https://doi.org/10.1002/2015GL064179

Revil, A. (2002). Genesis of mud volcanoes in sedimentary basins: A solitary wave-based mechanism. *Geophysical Research Letters*, *29*(12), 1574. https://doi.org/10.1029/2001gl014465

Revil, A., & Cathles, L. M. (1999). Permeability of shaly sands. *Water Resources Research*, *35*, 651–662.

Richard, G. C., Kanjilal, S., & Schmeling, H. (2012). Solitary-waves in geophysical two-phase viscous media: A semi-analytical solution. *Physics of the Earth and Planetary Interiors*, *198*, 61–66. https://doi.org/10.1016/j.pepi.2012.03.001

Richardson, C. N. (1998). Melt flow in a variable viscosity matrix. *Geophysical Research Letters*, *25*(7), 1099–1102. https://doi.org/10.1029/98gl50565

Sabitova, A. I., Yarushina, V. M., Stanchits, S. A., Stukachev, V. I., & Myasnikov, A. V. (2021). Experimental compaction and dilation of porous rocks during triaxial creep and stress relaxation. *Rock Mechanics and Rock Engineering*. https://doi.org/10.1007/s00603-021-02562-4

Sone, H., & Zoback, M. D. (2014). Time-dependent deformation of shale gas reservoir rocks and its long-term effect on the in situ state of stress. *International Journal of Rock Mechanics and Mining Sciences*, *69*, 120–132. https://doi.org/10.1016/j.ijrmms.2014.04.002

Stevenson, D. J. (1989). Spontaneous small-scale melt segregation in partial melts undergoing deformation. *Geophysical Research Letters*, *16*(9), 1067–1070. https://doi.org/10.1029/gl016i009p01067

Svensen, H., Planke, S., Polozov, A. G., Schmidbauer, N., Corfu, F., Podladchikov, Y. Y., & Jamtveit, B. (2009). Siberian gas venting and the end-Permian environmental crisis. *Earth and Planetary Science Letters*, *277*(3–4), 490–500. https://doi.org/10.1016/j.epsl.2008.11.015

Tian, M., & Ague, J. J. (2014). The impact of porosity waves on crustal reaction progress and CO_2 mass transfer. *Earth and Planetary Science Letters*, *390*, 80–92. https://doi.org/10.1016/j.epsl.2013.12.044

Vadakkepuliyambatta, S., Bunz, S., Mienert, J., & Chand, S. (2013). Distribution of subsurface fluid-flow systems in the SW Barents Sea. *Marine and Petroleum Geology*, *43*, 208–221. https://doi.org/10.1016/j.marpetgeo.2013.02.007

van Noort, R., & Yarushina, V. (2016). Water and CO_2 permeability of a shale sample core from Svalbard. *Energy Procedia*, *97*, 67–74. https://doi.org/10.1016/j.egypro.2016.10.021

van Noort, R., & Yarushina, V. (2019). Water, CO_2 and argon permeabilities of intact and fractured shale cores under stress. *Rock Mechanics and Rock Engineering*, *52*(2), 299–319. https://doi.org/10.1007/s00603-018-1609-8

Vilarrasa, V., & Makhnenko, R. Y. (2017). Caprock integrity and induced seismicity from laboratory and numerical experiments. *Energy Procedia*, *125*, 494–503. https://doi.org/10.1016/j.egypro.2017.08.172

Weaver, C. E. (1989). *Clays, muds, and shales* (p. 819): ElsevierDistributors for the U.S. and Canada, Elsevier Science Pub. Co.

Wissa, A. E. Z. (1969). Pore pressure measurement in saturated stiff soils. *Journal of the Soil Mechanics and Foundations Division*, *95*(4), 1063–1073. https://doi.org/10.1061/JSFEAQ.0001304

Wu, X. D., Zhang, Y., Zhang, K., Liu, B., Zuo, J. Y., Chen, G. J., & Xiao, P. (2021). An experimental investigation of liquid CO_2-in-water emulsions for improving oil recovery. *Fuel*, *288*, 288. https://doi.org/10.1016/j.fuel.2020.119734

Yang, D. S., Bornert, M., Chanchole, S., Wang, L. L., Valli, P., & Gatmiri, B. (2011). Experimental investigation of the delayed behavior of unsaturated argillaceous rocks by means of digital image correlation techniques. *Applied Clay Science*, *54*(1), 53–62. https://doi.org/10.1016/j.clay.2011.07.012

Yarushina, V. M., & Podladchikov, Y. Y. (2015). (De)compaction of porous viscoelastoplastic media: Model formulation. *Journal of Geophysical Research: Solid Earth*, *120*, 4146–4170. https://doi.org/10.1002/2014JB011258

Yarushina, V. M., Podladchikov, Y. Y., & Connolly, J. A. D. (2015). (De)compaction of porous viscoelastoplastic media: Solitary porosity waves. *Journal of Geophysical Research: Solid Earth*, *120*, 4843–4862. https://doi.org/10.1002/2014JB011260

Yarushina, V. M., Podladchikov, Y. Y., & Wang, H. (2020). Model for (de)compaction and porosity waves in porous rocks under shear stresses. *Journal of Geophysical Research: Solid Earth*, *125*, e2020JB019683. https://doi.org/10.1029/2020JB019683

Zhang, C. L., Rothfuchs, T., Su, K., & Hoteit, N. (2007). Experimental study of the thermo-hydro-mechanical behaviour of indurated clays. *Physics and Chemistry of the Earth*, *32*(8–14), 957–965. https://doi.org/10.1016/j.pce.2006.04.038